

## Article

# Mechanism Analysis and Process Inversion of the “7.26” Landslide in the West Open-Pit Mine of Fushun, China

HuaJun Meng<sup>1,2,3</sup>, Jihuan Wu<sup>1,4,\*</sup> , Chunshan Zhang<sup>1,2,3,\*</sup> and Kungang Wu<sup>1,2</sup>

<sup>1</sup> Institute of Geomechanics, Chinese Academy of Geological Sciences, Beijing 100081, China; mhjun521@cags.ac.cn (H.M.); wukungang2023@163.com (K.W.)

<sup>2</sup> Key Laboratory of Active Tectonics and Geological Safety, Ministry of Natural Resources, Beijing 100081, China

<sup>3</sup> Observation and Research Station of Geological Disaster in Baoji, Shaanxi Province, Ministry of Natural Resources, Beijing 100081, China

<sup>4</sup> Shenyang Geological Survey, China Geological Survey, Shenyang 110034, China

\* Correspondence: wujihuan97@163.com (J.W.); zhangcs401@sina.com (C.Z.)

**Abstract:** Mine landslides are geological disasters with the highest frequency and cause the greatest harm worldwide. This typically causes significant casualties and damage to property. The study of the formation mechanisms and kinematic processes of mine landslides is important for the prevention and control of mine geological disasters and mine production safety. This study examined the “7.26” landslide, which occurred in the West Open-pit Mine of Fushun, China, in 2016, based on detailed investigations, interferometric synthetic aperture radar (InSAR) monitoring, and numerical simulations. The mechanism of landslide formation was explored, its kinematic process was inverted, and its disaster evolution process was summarized. The results indicate that: (1) For the formation mechanism of the “7.26” landslide, in July 2015, the old sliding mass was reactivated and deformed along the dominant joints in the shale. The following year, owing to continuous rainfall during the rainy season, the sliding surface accelerated its connection. Finally, a rainstorm on 25–26 July 2016, triggered slope instability. (2) The process of continued movement after landslide instability was approximately 250 s. It can be divided into the landslide initiation (0–10 s), collision scraping (10–150 s), and accumulation stages (150–250 s). (3) The entire process of landslide disasters includes four stages. During the weak-deformation stage, the maximum deformation of the sliding mass monitored by InSAR was approximately 50 mm. During the strong deformation stage, the tensile cracks at the rear edge of the landslide continued to expand, and shear outlets at the front edge had already formed. During the instability and failure stages, rainstorms trigger slope instability, leading to landslides. During the sliding accumulation stage, the landslide mass transformed into debris flow along the slope surface and accumulated at the bottom of the pit. This study provides a theoretical basis for the subsequent evaluation, treatment, monitoring, and warning of landslides in the Fushun West Open-pit Mine and other deep excavation open-pit mines.

**Keywords:** open-pit mine; landslide; deformation and failure; genetic mechanism; kinematics; Fushun; China



**Citation:** Meng, H.; Wu, J.; Zhang, C.; Wu, K. Mechanism Analysis and Process Inversion of the “7.26” Landslide in the West Open-Pit Mine of Fushun, China. *Water* **2023**, *15*, 2652. <https://doi.org/10.3390/w15142652>

Academic Editors: Yuanjun Jiang and Heng Liang

Received: 1 June 2023

Revised: 15 July 2023

Accepted: 18 July 2023

Published: 22 July 2023



**Copyright:** © 2023 by the authors. Licensee MDPI, Basel, Switzerland. This article is an open access article distributed under the terms and conditions of the Creative Commons Attribution (CC BY) license (<https://creativecommons.org/licenses/by/4.0/>).

## 1. Introduction

On 22 February 2023, a large-scale collapse occurred on the slope of an open-pit coal mine in the Alaskan League, Inner Mongolia, northern China. This event caused many workers and vehicles to be buried, causing people to focus more on the prevention and mitigation of mine landslides. An open-pit mining slope is an open-slope system that has been reformed manually. It is characterized by a steep slope shape, densely developed weathering and unloading cracks, and weak and fractured slope rock masses [1]. Mine slope landslides are an important form of geological disaster caused by engineering activities and are an external manifestation of the mutual feedback mechanism between humans and

nature [2]. Mine landslides are one of the most frequent and harmful geological disasters worldwide. They typically result in severe casualties and property damage. For example, the Amynteon mine landslide in Greece caused approximately 180 residents to evacuate their homes and caused economic losses of approximately EUR 500 million [3]. The Las Cruces mine landslide in Spain caused the collapse of mine dumps and buried mining equipment and miners [4]. Landslide disasters exist in 80–90% of open pits in China [5]. This has significantly restricted the production and development of mines. A representative example is the Fushun West Open-pit Mine in Liaoning Province, China, which has aroused widespread concern from all circles of society [6,7]. This open-pit mining began in 1914, and the mine experienced its first pit slope collapse in 1927. To date, nearly a hundred recorded landslides of various sizes have been recorded in the mining areas. This poses a serious risk to the safety of workers in mine areas, surrounding industrial enterprises, and residents.

Extensive research has been conducted on controlling and preventing landslides in open-pit mines. Zhang et al. [7] proposed a comprehensive method based on microseismic monitoring and numerical simulations to evaluate the stability and reinforcement effects of landslides in deep excavation mines under complex stress conditions. An et al. [8] summarized the rainfall-seepage response characteristics and stability change mode of landslides in open-pit mines with faults induced by rainfall and proposed a mine landslide reinforcement system based on a high constant resistance and large deformation anchor cable. Kang et al. [9] established a quantitative relationship between the probability of a mine landslide and the parameters of rock mass strength, slope height, and slope angle and applied it to the analysis of rock landslides in the Chaarat gold mine. Systematic landslide prevention in open-pit mines remains a challenge. It includes various aspects, such as stability evaluation, engineering prevention and control, monitoring, and early warning research. The implementation of various tasks relies on a deep understanding of the formation mechanism and disaster process of mining landslides [10–12], which helps guide the prevention and reduction of landslide disasters in mining areas, reduce landslide risks, and ensure the safety of disaster-bearing bodies.

Therefore, the “7.26” landslide on the north side of the Fushun West Open-pit Mine that occurred in 2016 is taken as the research object. Based on field investigations and small baseline subset interferometric synthetic aperture radar (SBAS-InSAR) surface deformation monitoring technology, the genetic mechanism of this landslide is comprehensively analyzed using geological structure characteristics, historical landslide events, and rainfall excitation conditions. Massflow numerical analysis is used to invert the kinematic process and motion characteristics of the landslide, providing a basis for evaluation, prevention, and monitoring of landslides in open-pit mines.

## 2. Overview of the “7.26” Landslide

### 2.1. Geological Background of Landslide Occurrence

The Fushun West Open-pit Mine is located in Fushun City, Liaoning Province, China. The “7.26” landslide occurred in the middle of the slope on the north side of the mine, as shown in Figure 1. The open-pit mine is approximately 6.8 km long, 2.2 km wide, and 10.8 km<sup>2</sup> in area.

The mine is located in the control area of the Hunhe fault. The strata on the north side of the mining area are primarily Cretaceous sandy conglomerates, Paleogene mudstone, shale, and coal. The main fault,  $F_1$ , of the Hunhe Fault along with its traction syncline are the main disaster-control structures on the northern slope.  $F_1$  is a right-handed thrust fault. Its occurrence is  $340\text{--}355^\circ \angle 60\text{--}80^\circ$ , and its crushing bandwidth is approximately 30–70 m.  $F_1$  enters from the northwest side of the pit, cuts the north slope obliquely, and crosses from the position of “7.26” landslide, which is effective in controlling the landslide on the northern side. The occurrence of the axial surface of the traction syncline is  $310\text{--}325^\circ \angle 50\text{--}60^\circ$ , and the northern wing of the syncline is steeper than the southern wing. This has led to the inversion of the Paleogene coal-bearing strata, which, together

with the  $F_1$  fault and Cretaceous strata, constitute the main part of the high soft rock slope to the north. The height of the north slope is approximately 420 m, and the slope angle is  $25\text{--}34^\circ$ , as shown in Figure 2.

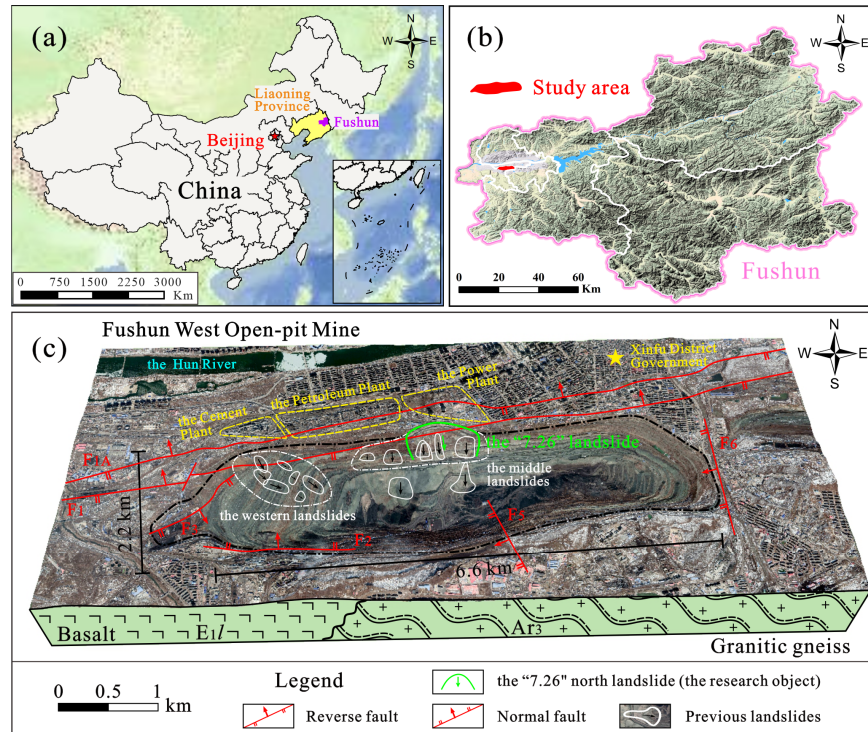


**Figure 1.** General situation of the research area. (a) Regional location map of Fushun City; (b) regional location map of Fushun West Open-pit mine; (c) overview of geological hazards in mining area.

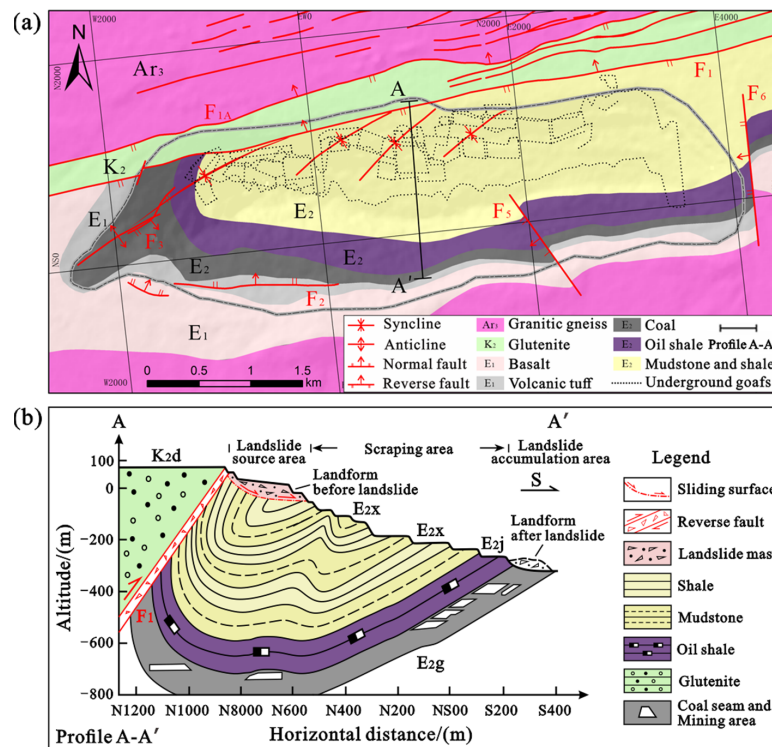


**Figure 2.** Engineering geological profile of the north slope. (a) Geological map of open pit mine; (b) geological profile of North Slope of mine pit.

Controlled by regional tectonic movement, the structural planes in the north slope are dense, cutting and fracturing rock masses and resulting in the development of water conduction cracks. In addition, the mudstone and shale, which form the main part of the slope, are significantly softened by groundwater infiltration. Affected by large-scale open-pit combined mining, the core of the syncline was stripped, and weathering and unloading in the rock mass were evident. The quality of the rock mass in the shallow part of the slope has grades III–V [13]. Under the internal and external dynamic geology, the north slope was extremely susceptible to landslides, as shown in Figure 1c.

## 2.2. Deformation and Failure Characteristics of Landslide

A detailed investigation of the landslide area indicates that the “7.26” landslide is in the upper part of the middle section of the northern slope. The main sliding direction was  $174^\circ$ . The landslide is approximately 300 m long from north to south. The rear edge of the landslide extended north to the railway garage, and the front edge extended south to the 12th trunk railway in the mining area. The landslide is approximately 560 m wide from east to west. The east and west walls of the landslide are opposite each other. The sidewalls are steep in the west, gentle in the east, steep in the upper part, and gentle in the lower part, forming an asymmetric landslide wedge-shaped double-sliding surface. The elevation distribution of landslide mass is approximately  $-25$  to  $+75$  m, high in the north and low in the south. The distribution area of the landslide mass was approximately  $15 \times 10^4$  m<sup>2</sup>, an average thickness of approximately 35 m and a scale of approximately  $313 \times 10^4$  m<sup>3</sup>. The landslide mass was primarily composed of mudstone and shale. After the first sliding of the mudstone and shale, the small-scale fault fracture zone and gravel-rock formations in the upper part were unable to maintain their own stability owing to a lack of support and were forced to participate in the sliding, as shown in Figure 2. Overall, the landslide was a large-scale rock wedge landslide. The landslide damaged two railways, four roads, and 20 buildings within the northern boundary, causing direct economic losses of approximately CNY 17.8 million, as shown in Figure 3.

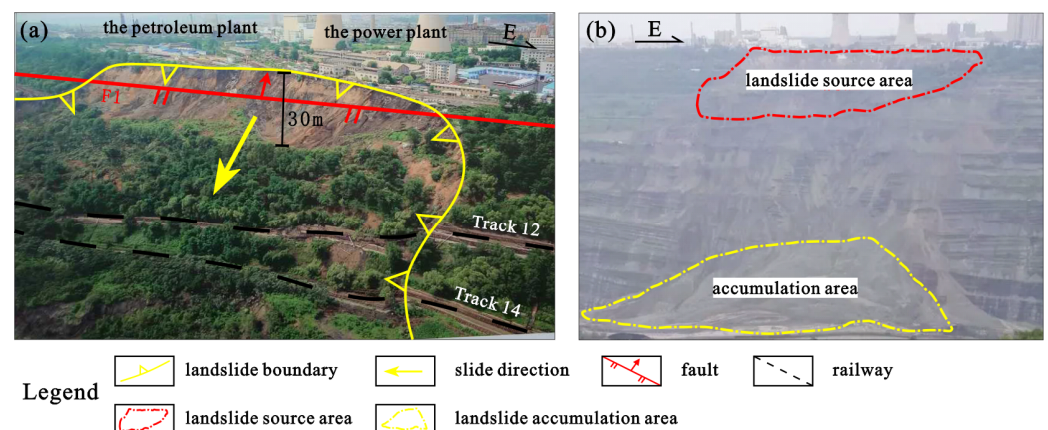


**Figure 3.** Deformation and failure characteristics of the “7.26” landslide. (a) Aerial photograph of landslide source area; (b) aerial photograph of landslide and its hazard area.

After the “7.26” event, the landslide area at the top of the northern slope presented a typical “circular chair shaped” landform. The rear edge of the landslide was pulled approximately 20 m apart. The rear wall of the landslide formed a steep slope with a height of approximately 30 m, with the upper part of the alluvial layer being steep and the lower part of the sandstone being gentle. The maximum height difference of the steep slope on the western side of the landslide was approximately 15 m. The sliding mass on the west side had a relatively large displacement distance, and there were no complete steps. Multiple echelon feather-shaped shear fractures have developed. The eastern boundary of the landslide exhibited a small drop, and local steps could still be identified in the nearby landslide body, which rotated at a certain angle. Several east–west trending feather

shaped cracks formed on both sides of the landslide mass. The upper part of the landslide body appeared as a steep slope with a depression at the rear edge. There were east–west transverse and north–south longitudinal cracks in the middle of the landslide. This was caused by the internal differential movement of the landslide mass during sliding. High and steep steps of loose rock formed at the front edge of the landslide. The sliding rocks, except for a few buried railway residues at the  $-24$  m level, turned into debris flow and slid to the bottom of the pit, as shown in Figure 3b.

### 3. Analysis of Landslide Mechanism

The slope where the “7.26” landslide is located has a fractured rock mass structure and good free surface conditions. Multiple slope instability events have occurred in this region [14]. The history of landslides can be traced to small-scale wedge sliding that occurred in April 1978. Subsequently, in August 1993, the largest landslide occurred within the northern boundary at a scale of approximately  $450 \times 10^4$  m<sup>3</sup>. The “7.26” landslide is a disaster event that occurred in the “1993.8” landslide area. In addition, the “7.26” landslide followed a rainstorm event in the rainy season of 2016. The promoting effect of atmospheric precipitation on landslide development is significant [15]. The study area receives concentrated rainfall from May to August each year, accounting for approximately 71.7% of the total annual rainfall. Most landslides in mining areas are induced by rainfall [16]. Therefore, the cause of the “7.26” landslide was that an old landslide controlled by a weak structural plane, which is triggered by strong rainfall, lost stability again, leading to the landslide. This viewpoint can be proven by a subsequent analysis of the structural characteristics of the landslide areas and the development law of deformation before sliding.

#### 3.1. Control of Weak Structural Planes

The viewpoint that the “7.26” landslide was controlled by weak structural planes can be proven by the structural characteristics of the landslide area. As shown in Figure 3a, the northward-dipping  $F_1$  fault intersects at a small angle with the rear edge of the “7.26” landslide and then deviates from the mining area. Controlled by  $F_1$ , the rear wall of the landslide was adjacent to the fault. The sliding zone was broken by a fault and did not connect to the upper sandstone conglomerate, thus limiting the main body of the landslide to the mudstone and shale layers. In addition to faults, a series of joint fissures associated with the Hunhe Fault affected the deformation and instability of the slope. Owing to the control effect of the rock mass structure [17], the joint surfaces inclining towards the outside of the slope play a significant role in the formation of rock landslides on the mining slope. Mudstone and shale layers are the main disaster-prone strata of this landslide. According to the statistics, three groups of dominant joints developed in the mudstone and shale interbedded intervals on the northern slope [18], as shown in Table 1. The first and second groups of joints have similar occurrences as the two sides of the “7.26” landslide. It also has a steep eastward-dipping interface and a gentle westward-dipping interface. This indicates that the lateral boundary of the sliding wedge was controlled by these two sets of joints and later developed and expanded along their tracks.

**Table 1.** Main joints in mudstone and shale strata.

Number of Joint Groups	Occurrence	Joint Density (bar·m <sup>-1</sup> )
Joint group 1	130–145° ∠ 40–75°	3–5
Joint group 2	220–230° ∠ 40–50°	1–2
Joint group 3	248° ∠ 67°	1–3

By comparing the intersections between weak structural planes, such as secondary dominant joints and synclinal fold bedding in mudstone and shale, and the northern slope surface, a slope stability analysis based on stereographic projections was conducted, as shown in Figure 4. From the perspective of rigid-body mechanics, when considering only the sliding and anti-sliding forces of the deformed rock mass of the slope, the different

degrees of northward inclination of the two wings of the syncline did not have a significant negative impact on the stability of the north slope. However, among the 12 sets of wedge-shaped rock block contour boundary lines formed by three sets of joint cutting within the rock layer, one set caused critical instability in the local steep steps of the mining slope, while the other five sets caused local instability of the slope, accounting for 28.57% of the total intersection lines of the primary and secondary structural planes. The intersections of the first and second sets of joints in mudstone and shale are among the unstable contour lines, proving that the formation of the “7.26” landslide body is controlled by the weak structural planes inside the soft rock strata.

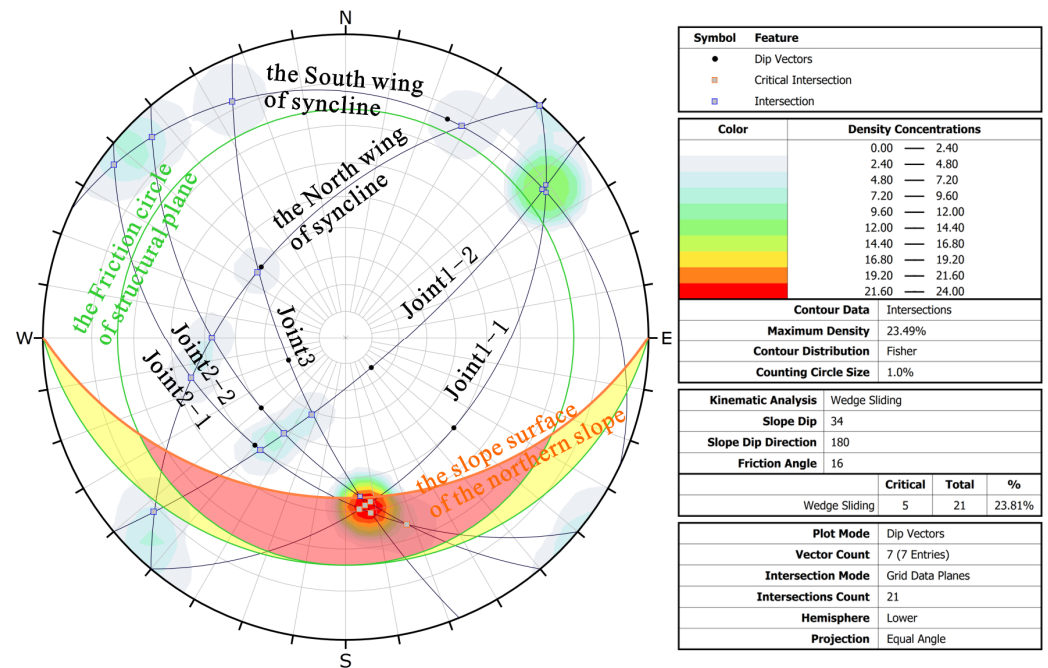
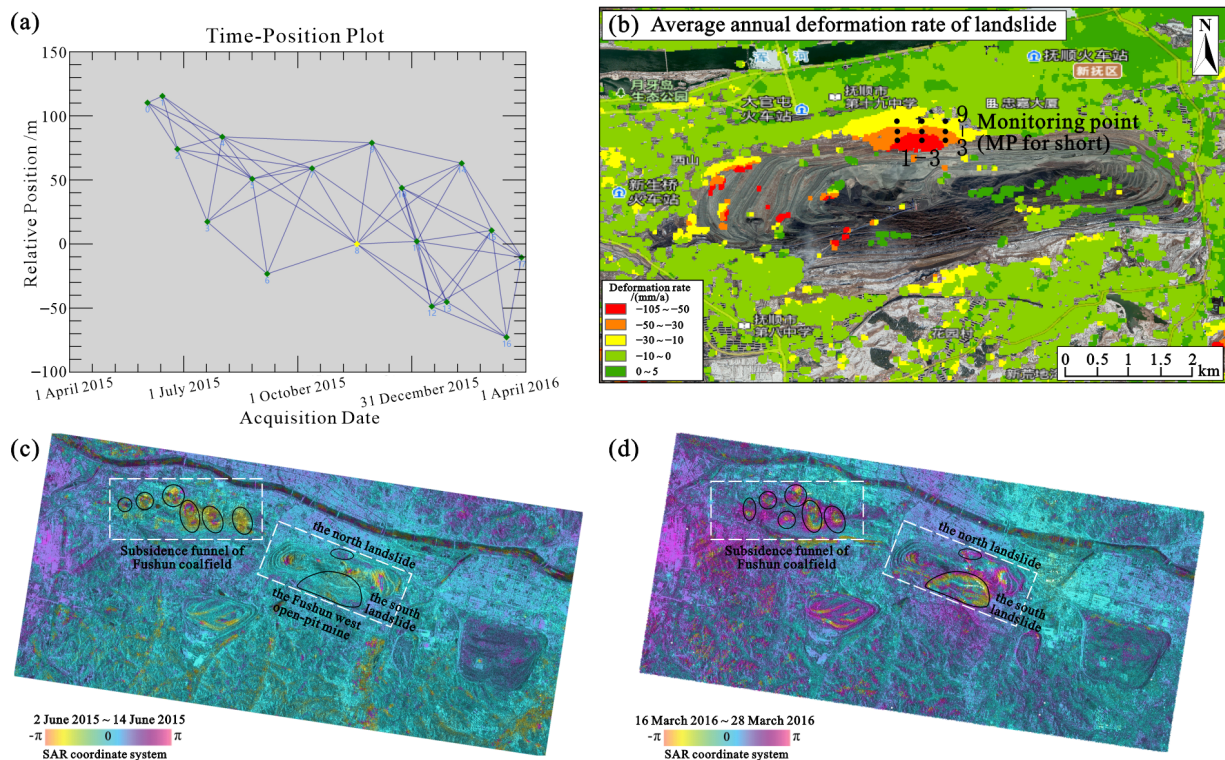


Figure 4. Stereographic projection analysis of the north slope.

### 3.2. Revival of Historical Landslides

According to research by Gao Bo et al. [14], in August 1993, the large-scale sliding deformation zone was located along the E800–E1300 section on the north slope of the Fushun West Open-pit Mine at an elevation of −30–75 m. The scope is greater than the “7.26” landslide. The front edges, side walls, and perimeter positions of the two landslides were consistent. Therefore, SBAS-InSAR technology was used to analyze the pre-slip deformation of the 1993 old landslide (also known as the “7.26” landslide area) to prove that the “7.26” landslide is a revival of historical landslides. To ensure the pertinence of the research and control the variables, the monitoring time series was limited to the landslide deformation stage before the rainy season in 2016, thereby removing the interference caused by “rainfall triggering.” The monitoring and analysis of the early deformation time series of the “7.26” landslide collected 18 rounds of Sentinel-1A orbital interferometric wide (IW) mode satellite data from June 2015 to March of the following year. Through interference and combination, the dataset comprises 72 sets of image pairs. The spatiotemporal baseline is shown in Figure 5a, with a time baseline threshold of 50 days and a spatial baseline threshold of 90 m. Simultaneously, in conjunction with the SRTM-30 m resolution digital elevation model (DEM), the leveling effect was removed.



**Figure 5.** SBAS-InSAR monitoring of the “7.26” landslide along the north slope before sliding. (a) Time-position plot of SBAS-InSAR; (b) average annual deformation rate of landslide; (c) SBAS-InSAR difference results in June 2015; (d) SBAS-InSAR difference results in March 2016.

The interference fringe patterns from one year (June 2015) to the rainy season before the landslide year (March 2016) were compared, as shown in Figure 5c,d. There are obvious signs of deformation around the “7.26” landslide. The general subsidence rate of the north slope during this period was approximately 10–30 mm/a, and the maximum deformation rate exceeded 50 mm/a, as shown in Figure 5b. In addition, the maximum deformation rate of  $-105$  mm/a in the figure occurred in the landslide on the south side of the mining area. This is not within the research area and will not be discussed in detail here. The landslide had already revived at this time and was exhibiting weak creep (sliding) deformation. Because the deformation rate of the front edge of the landslide was significantly higher than that of the rear edge, its movement trend under self-weight was of the traction type. This indicated that the mudstone-to-shale ratio in the lower part of the old landslide advanced into the plastic stage. This phenomenon is likely related to external loads, such as long-term mining disturbances, locomotive dynamic loads, and groundwater infiltration, which accelerate weathering and reduce strength. Nine deformation monitoring points were arranged inside and outside the landslide perimeter for subsequent analyses, as shown in Figure 5b.

The quarterly monitoring of the cumulative variables in the study area during this period is shown in Figure 6a. This study found no significant subsidence on the northern side of the mine during the first double-differential interference in June 2015. However, signs of continuous settlement and deformation began in September 2015. From the cumulative settlement amount in the following six months, the cumulative amount was essentially the same every quarter, and the overall settlement increased linearly. During this period, the settlement concentration area exhibited a southward development trend. Further analysis showed that the boundary of the deformation zone was clear, and there were graded differences in the deformation amount. There was a linear decreasing trend from south to north, with a cumulative subsidence of approximately 35–50 mm at the front edge of the landslide mass and less than 15 mm at the rear edge and side walls. Using

the deformation curves at the monitoring points, as shown in Figure 6b, there was no deformation at any point before 20 July 2015. However, on 1 August, the curve deflected downwards, indicating that the revival of the old landslide began in late July 2015. In the subsequent observation process, the slope of the deformation curve remains unchanged, indicating that the landslide is in a uniform deformation stage. This proves that the old landslide was revived before entering the rainy season of 2016.

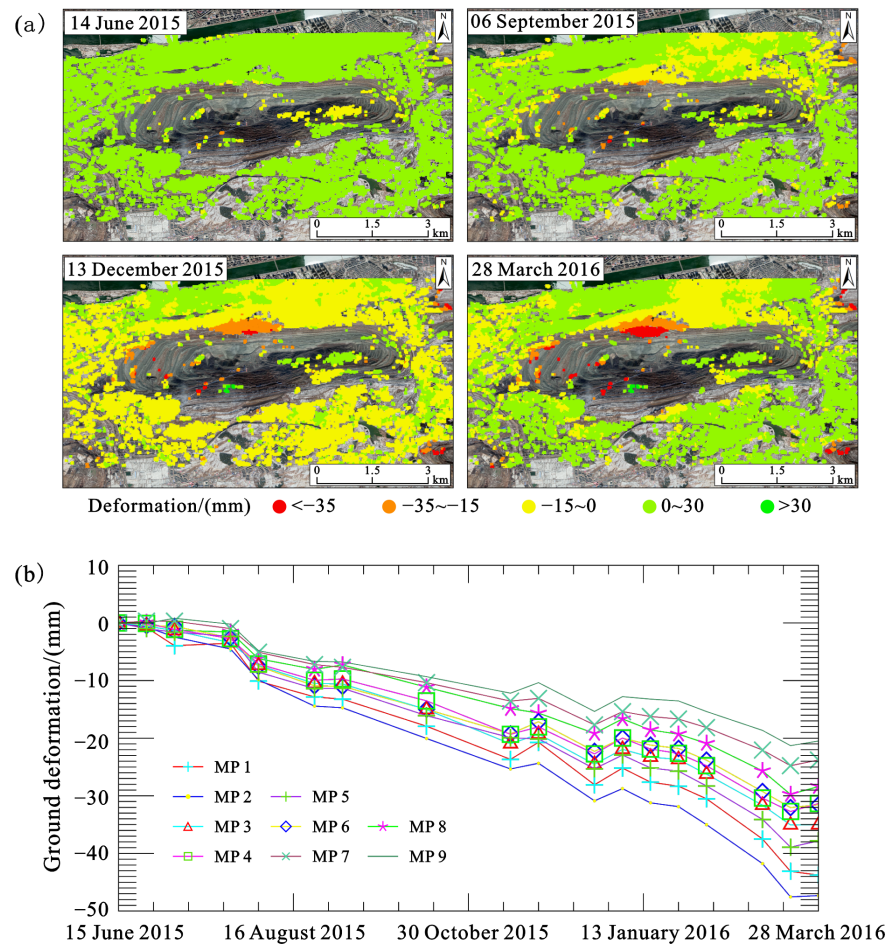
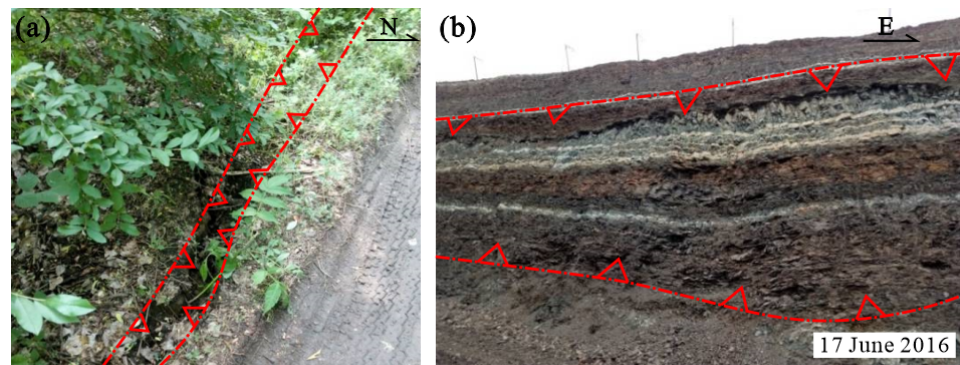


**Figure 6.** Deformation monitoring results of the “7.26” landslide on the north slope before sliding. (a) Surface deformation at different times; (b) Surface deformation curve of landslide monitoring points.

### 3.3. Continuous Rainfall Promotes Sliding, Extreme Rainfall Triggers Landslides

In May 2016, the Fushun area entered the rainy season, and continuous rainfall caused water to fill the interior of the slope. From May to July, the groundwater level in the study area increased by 77, 190, and 143 mm, respectively [19]. This caused effects such as ① fissure water filling and increased uplift pressure; ② rainwater infiltration and outward seepage force; ③ softening of rock mass, argillization of structural planes, and reduction in the shear strength of shale rock, which are not conducive to slope stability. On 17 June, tension cracks further developed in the E800–E1300 area of the original Xingping Road, with a length of approximately 20 m and a width of approximately 40 mm, as shown in Figure 7a. Near the 12th trunk railway on the front edge of the landslide, the shear outlet was formed, with visible scratches, as shown in Figure 7b. These signs indicate that the landslide entered an accelerated deformation or critical sliding stage, indicating that the sliding surface accelerated its development after the rainy season, and continuous rainfall promoted the development of the landslide.



Legend  Signs of landslide

**Figure 7.** Landslide signs in strong deformation stage during the rainy season. (a) Tension cracks at the rear edge of the “7.26” landslide; (b) shear outlet at the front edge of the “7.26” landslide.

Rainfall during the landslide month (July) peaked during the 2016 rainy season. Approximately four rainstorm days occurred, and the cumulative rainfall was 350 mm, accounting for 31.5% of the annual rainfall, as shown in Figure 8. During 25–26 July of that year, the Fushun West Open-pit Mine encountered a once-in-50-years heavy rainstorm, with precipitation reaching 176.3 mm. At approximately 5 a.m. on the 26th, a landslide occurred in the E800–E1300 section of the northern slope. This reflected the role of extreme rainfall in triggering landslides.

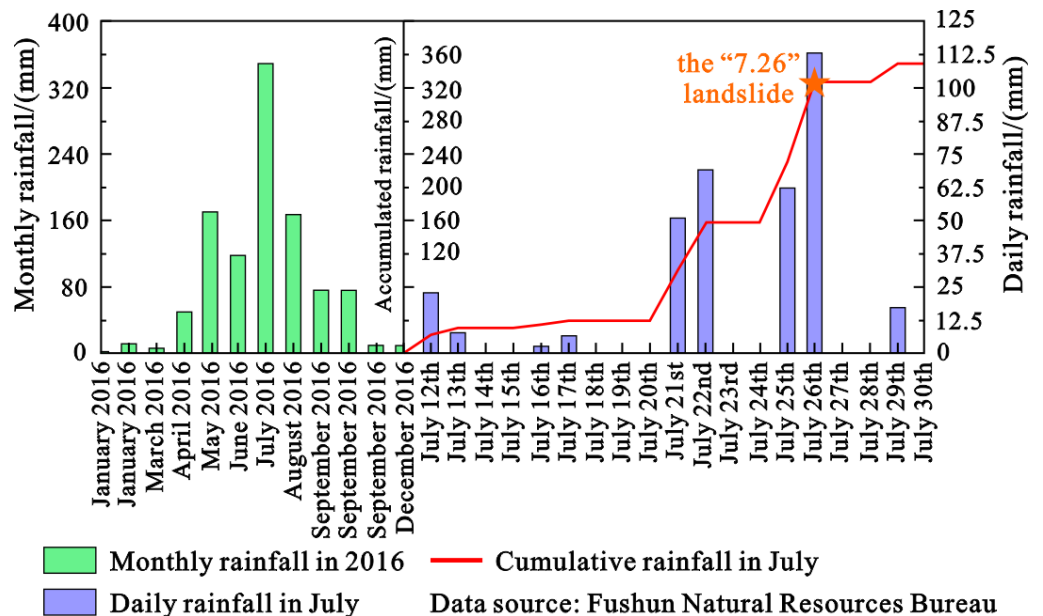


**Figure 8.** Monthly rainfall in 2016 and daily rainfall in July at the mine.

Based on the structural characteristics of the landslide source area and the deformation characteristics before the landslide, the formation mechanism of the “7.26” landslide can be summarized as follows: First, the mudstone and shale of old landslide bodies gradually revived, owing to gravity along the weak structural planes composed of two sets of dominant joints, and were in a slow creep stage. During the rainy season, it continued to transition to a strong deformation stage due to the influence of precipitation. Finally, triggered by rainstorms, stability became difficult to maintain, and a large-scale landslide event occurred.

#### 4. Inversion of the Landslide Kinematic Process

The complete evolution of landslides includes three stages: slope deformation, slope instability failure, and continued movement after slope failure [20]. The previous study analyzed the pre-slide deformation stage and destabilization failure stage of the “7.26” landslide and summarized the deformation and failure mechanism of the north slope in the source area. To better understand the entire development and evolution of landslides in open-pit mines and guide safety precautions against geological disasters in mine areas, this study investigated the kinematic process of landslides after slope destabilization.

##### 4.1. Landslide Simulation and Model Validation

In this study, the kinematic processes of a landslide were simulated using MassFlow. In this numerical analysis method, the conservation of the mass and momentum of the moving fluid are controlled by a generalized depth integral continuum mechanical model. The MacCormack-TVD finite-difference algorithm was combined with OpenMP and MPICH technologies to improve the speed of the solution. It has the advantages of an adaptive solution, second-order accuracy, the ability to capture discontinuous interfaces of multiphase flows, and basement erosion model characteristics [21,22].

The characteristics of landslide movement are affected by the material of the medium, morphology, and scale of the landslide mass, as well as the topography of the foundation. Therefore, the calculation parameters were set as follows:

1. Base friction model: Based on Ouyang et al. [22,23], the Coulomb friction model was selected to describe the objective of this study. The model is suitable for the simulation of debris flow disasters, such as landslides and rock collapses, and is expressed as follows.

$$\tau = c + \rho gh (1 - \lambda) \tan \varphi \quad (1)$$

where  $\tau$  is the foundation friction stress (kPa),  $c$  is the cohesive force (kPa),  $\rho$  is the density of the landslide mass ( $\text{kg}\cdot\text{m}^{-3}$ ),  $g$  is the gravitational acceleration ( $\text{m}\cdot\text{s}^{-2}$ ),  $h$  is the thickness of the landslide mass (m),  $\lambda$  is the pressure coefficient of the excess pore water, and  $\varphi$  is the internal friction angle ( $^{\circ}$ ).

2. Physical and mechanical parameters of rock and soil mass: Based on the physical and mechanical test results of rock and soil in the landslide mass and landslide zone, and referring to the probability model of parameter selection based on uniform distribution by Zhou et al. [24], after several trial calculations, the parameters of the landslide simulation calculation were determined, as listed in Table 2.
3. Landslide source: Through field investigation, remote sensing interpretation, and comparative analysis of the 1:2000 geological profile of the north slope before and after the landslide, the plane range of the source area of the landslide was found to be approximately  $201,620.9 \text{ m}^2$ , and the thickness of the landslide mass was approximately 0–44.7 m.
4. Base topography: The base sliding bed topography was established using the ALSO-12.5 m DEM. The model was 6.6 km long and 2.2 km wide. Considering calculation accuracy and effectiveness, a range of approximately  $2 \text{ km} \times 1.5 \text{ km}$  in the middle of the mine was selected as the calculation area. A total of 83,250 structured grids were divided into 6 m intervals. The model was run for 250 s, and the calculation time step was limited to  $\Delta T < 1 \text{ s}$ .

**Table 2.** Calculation parameters of the “7.26” landslide simulation.

Density of Landslide Mass ( $\rho$ )	Internal Friction Angle ( $\varphi$ )	Cohesive Force ( $c$ )	Pressure Coefficient of Excess Pore Water ( $\lambda$ )	Gravitational Acceleration ( $g$ )
$2250 \text{ kg}\cdot\text{m}^{-3}$	$16.0^{\circ}$	85 kPa	0.75	$9.8 \text{ m}\cdot\text{s}^{-2}$

The field investigation determined that the “7.26” landslide has good free surface conditions and sufficient sliding space. This facilitated the potential energy-to-kinetic energy conversion of the landslide mass after shearing from the front edge. When the rock and soil body slides down the slope to the bottom of the pit, movement is blocked and accumulates, and the bottom of the pit is cut into eastern and western sections. The simulation results for the landslide movement process are shown in Figure 9. The final accumulation characteristics of the simulated landslide were consistent with the experimental results. A quantitative comparison showed that the simulation accuracy was higher than 82.65% (Table 3), which confirmed the reliability of the simulation results and subsequent analysis [25,26].

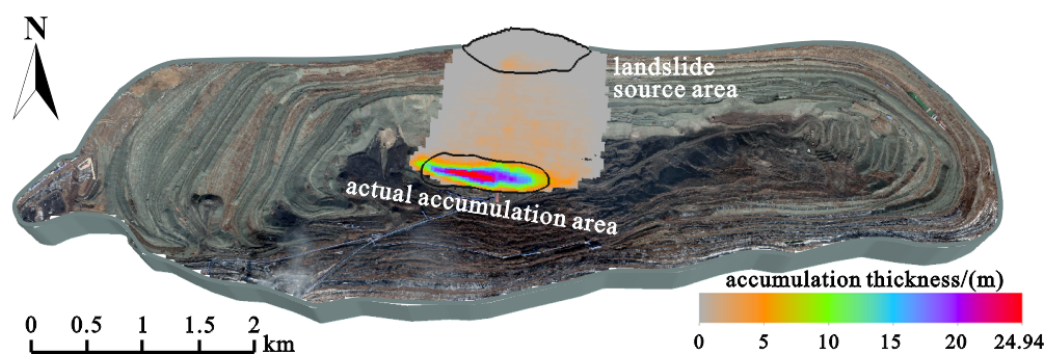


Figure 9. “7.26” Landslide simulation results.

Table 3. Validation of the “7.26” landslide simulation results.

The “7.26” Landslide	Simulated Calculation Value	Survey Values	Pressure Coefficient of Excess Pore Water (%)
Accumulate area (m <sup>2</sup> )	219,562.15	187,105.72	17.35
Maximum thickness of accumulation (m)	24.94	28.35	12.02

#### 4.2. Kinematic Process Analysis

The “7.26” landslide motion inversion results are shown in Figures 10 and 11. The entire movement of the landslide lasted 250 s. The landslide mass accumulated within approximately 200 s. The movement path extended from the top of the north slope to the bottom of the pit. The maximum sliding distance of the landslide was approximately 660 m, and the height difference was approximately 320 m. The maximum downslope speed was 10.2 m/s, making this a high-speed landslide. The movement process can be divided into three stages:

##### 1. Landslide initiation stage

The starting stage of the landslide occurred from 0–10 s. The landslide slid along the inclined direction of the slope, with a main sliding direction of 174°. The apparent friction angle was 18.43°. At this stage, the acceleration of the landslide was complete, and both its center of gravity and velocity reached the front of the landslide source area. In terms of energy, the primary focus was on the conversion of potential energy into kinetic energy and the generation of heat through sliding bed friction.

##### 2. Collision scraping stage

The crash scraper stage occurred from 10 to 150 s. During this stage, the landslide gradually sheared from the front edge of the landslide area. The sliding mass first collided with the step of the slope and then scraped it; therefore, it disintegrated and moved as a debris flow. Then, it slid along the high and steep mudstone and shale slopes at the lower part of the north slope and reached the bottom of the pit first in the front section at approximately 150 s. At this stage, the speed of the sliding body first increased and

then decreased. At approximately 50 s, the sliding speed reached its peak value and not the entire process of continuous acceleration. This indicates that the debris flow gradually accelerated in the early stage by gravity and gradually decelerated in the late stage due to friction. Friction is generated by the impact of the slider on the sloped surface of the scraper.

### 3 Landslide accumulation stage

The stacking stage occurred from 150–250 s. The stacking morphology process shows that after sliding for 200 s, the morphology of the stacking body stabilized. No significant changes were observed during subsequent exercises. When the final movement ceased, the landslide accumulation formed an oval shape. The maximum depth of the accumulation was approximately 24.9 m, the width was approximately 120 m, and the length was approximately 500 m. In addition, a small portion of the landslide remained on the slope surface and landslide source area, which was consistent with the actual situation. Based on the trend of the sliding speed, as shown in Figure 11, at this stage, the sliding body can be divided into two parts based on the different sliding directions. In other words, the rear sliding body slowly reached the bottom of the pit, and the front sliding body collided with the rebound pile on the southern slope. At this time, owing to the high accumulation of the central sliding body and the narrow terrain in the middle before the pit-bottom sliding, the accumulation body gradually shifted westward.

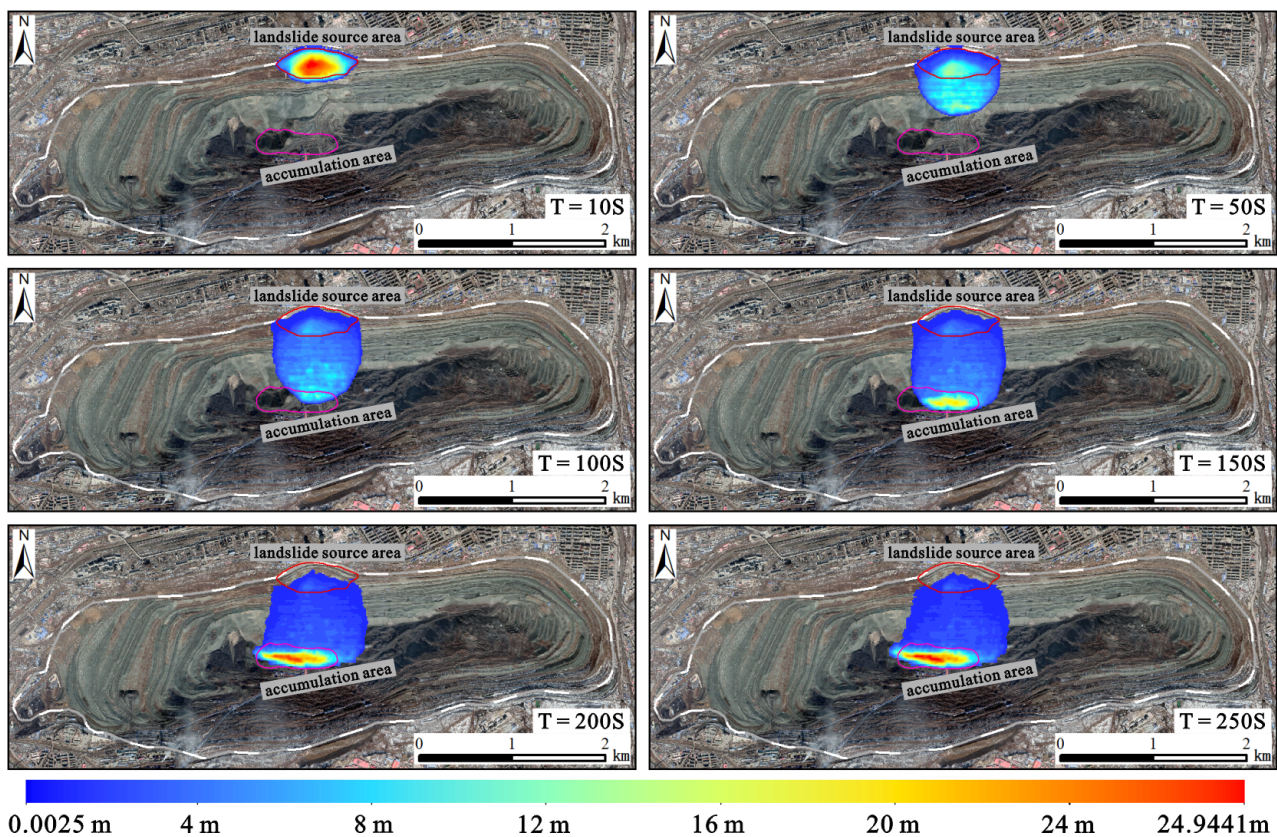


Figure 10. Accumulation of the sliding body at different times.

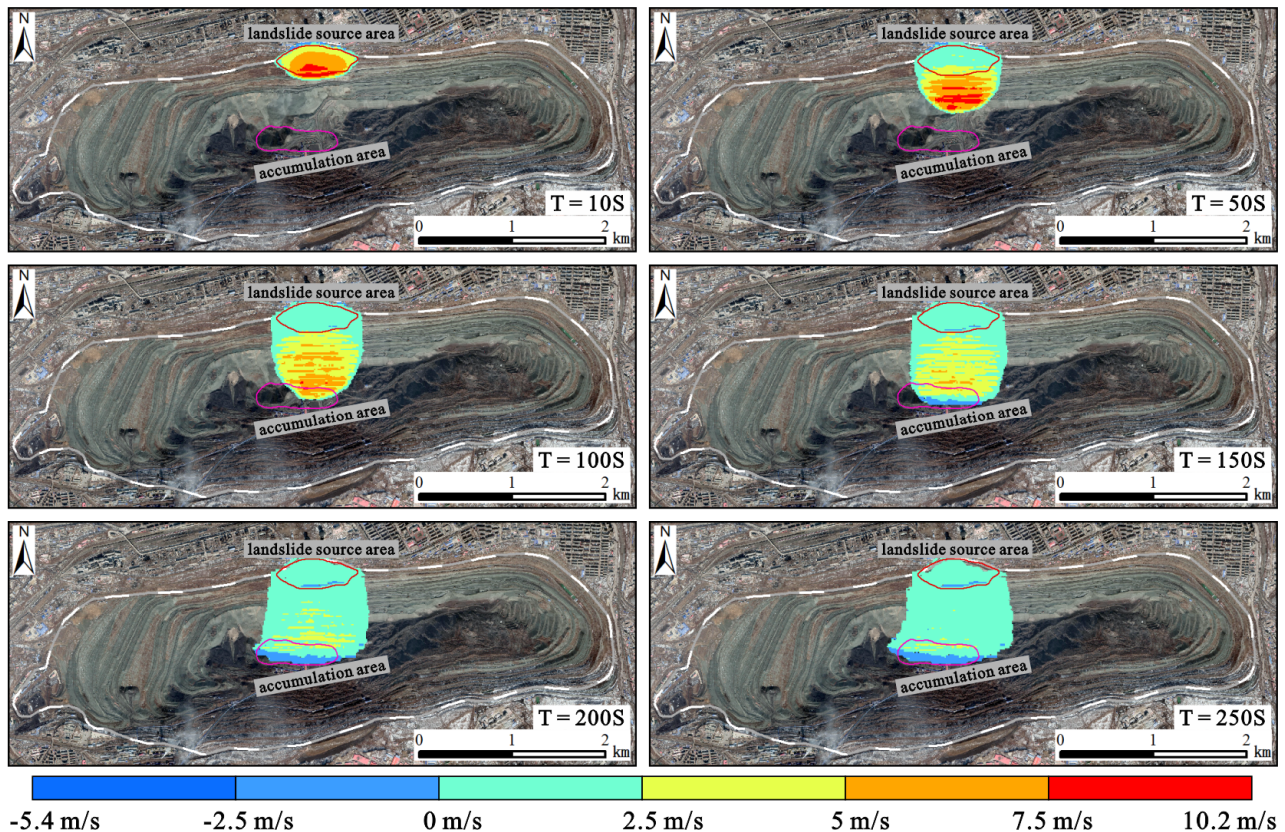


Figure 11. Speed of the sliding body at different times.

## 5. Discussion

The entire process of “7.26” landslide disaster in the Fushun West Open-pit Mine can be summarized as follows:

- Owing to long-term gravity and weathering, the old landslide mass at the top of the north slope was reactivated in late July 2015 and crept along two groups of controlled structural planes in the mudstone and shale formations. This corresponds to the weak deformation stage.
- After the 2016 rainy season, continuous rainfall increased the uplift pressure and permeability of the cracks and decreased the strength of mudstone and shale. The tensile crack at the rear edge of the landslide accelerated, and a shear outlet formed at the front edge. This is the stage of strong deformation.
- Until July 26, the mine suffered a once-in-50-year rainstorm. The cracks at the rear edge of the landslide were filled with water. The hydrostatic pressure at the rear edge was pointing out of the slope, and that of the seepage field inside the slope increased sharply. The sliding surface passed through. The old landslide mass at the top of the slope was destabilized. This is the stage of destabilization and destruction.
- After the landslide occurred, the sliding mass was sheared from the front edge. The landslide mass in the middle and lower sections transformed into a debris flow along the slope. The debris scraped and shoveled the slope surface, causing damage and a downward step migration. The top of the north slope formed a circular chair-shaped landslide depression. When the high-speed part of the debris flow first reached the bottom of the pit, movement at the foot of the southern slope was hindered, and kinetic energy dissipated. The subsequent slow parts gradually arrived and accumulated at the bottom. Terrain with high middle and low east–west was initially formed at the bottom of the mine pit. The movement ended at this point. This is the stage of sliding accumulation.

## 6. Conclusions

Landslides are among the greatest potential hazards in open-pit mining areas. This study took the “7.26” landslide of the Fushun West Open-pit Mine as an example. Through a detailed investigation, InSAR monitoring, and numerical simulation, the formation mechanism and disaster formation process of landslides were studied. The main conclusions are as follows.

- (a) The “7.26” landslide was caused by a weak structural plane, pre-existing old landslide mass, and seasonal rainfall. It gradually evolved from a steady state to destabilization in a certain sequence of main control. The rainy season of 2016 was used as the time boundary. The early stage was the reactivation of a wedge-shaped old landslide mass jointly controlled by the Hunhe Fault ( $F_1$ ) and the dominant joints of mudstone and shale. In the later stages, continuous rainfall accelerated the deformation of the landslide, causing a rainstorm-induced landslide event.
- (b) The movement process of the “7.26” landslide after destabilization can be divided into (1) the starting stage (0–10 s): the slope was unstable, and the landslide was cut from the front edge; (2) the stage of impact scraping (10–150 s): the landslide mass disintegrated after collision, turning into a debris flow and scraping the slope surface; and (3) the accumulation stage (150–250 s): arriving at the bottom of the pit, movement was blocked and gradually accumulated.
- (c) The entire disaster-causing process of the “7.26” landslide can be summarized as follows: (1) weak deformation stage: creep of an old landslide mass occurred along weak structural plane under gravity; (2) strong deformation stage: continuous rainfall gradually muddied the controlled structural plane, forming shear outlet; (3) instability and failure stage: triggered by rainstorm, the sliding surface was continuous, and the landslide mass became unstable; (4) sliding accumulation stage: the landslide mass transformed into debris flow along the slope surface and accumulated at the bottom of the pit.

Only one example, a mine landslide, is discussed in this study. Despite their distinctive features, this type of landslide has not been fully represented. In a follow-up study, it is necessary to summarize the types of landslides in open-pit mines and analyze the catastrophic mechanism and evolution process of landslides in various mines to guide mine safety prevention.

**Author Contributions:** Methodology, H.M.; project administration, H.M.; funding acquisition, H.M.; writing—original draft, H.M. and J.W.; data curation, J.W.; writing—review & editing, C.Z.; formal analysis, C.Z.; supervision, C.Z.; investigation, K.W. All authors have read and agreed to the published version of the manuscript.

**Funding:** This research was funded by the National Natural Science Foundation of China (grant number 42130720), the Geological Survey Project of CGS (grant number DD20190318, DD 20221816 and DD20230437), and the Shenyang Science and Technology Talent Project (grant number RC220450).

**Data Availability Statement:** Data not available due to legal restrictions. Due to the nature of this research, participants of this study did not agree for their data to be shared publicly, so supporting data are not available.

**Acknowledgments:** The authors thank the Bureau of Natural Resources of Fushun City and the 10th Geological Brigade of Liaoning Province for providing the rainfall data in the Fushun area and the 1:2000 geological profile before and after the “7.26” landslide, which were of great help to the research.

**Conflicts of Interest:** The authors declare no conflict of interest.

## References

1. Froude, M.J.; Petley, D.N. Global fatal landslide occurrence from 2004 to 2016. *Nat. Hazards Earth Syst. Sci.* **2018**, *18*, 2161–2181. [[CrossRef](#)]
2. Bobrowsky, P.T.; Brian, M. *Encyclopedia of Engineering Geology*, 1st ed.; Springer: Cham, Switzerland, 2018; pp. 579–580. [[CrossRef](#)]

3. Karagianni, A.; Lazos, I.; Chatzipetros, A. Remote Sensing Techniques in Disaster Management: Amynteon Mine Landslides, Greece. In Proceedings of the Gi4DM: GeoInformation for Disaster Management Conference, Istanbul, Turkey, 18–21 March 2018. [[CrossRef](#)]
4. López-Vinielles, J.; Ezquerro, P.; Fernández-Merodo, J.A.; Béjar-Pizarro, M.; Monserrat, O.; Barra, A.; Blanco, P.; García-Robles, J.; Filatov, A.; García-Davalillo, J.C.; et al. Remote analysis of an open-pit slope failure: Las Cruces case study. Spain. *Landslides* **2020**, *17*, 2173–2188. [[CrossRef](#)]
5. Wei, Z.A.; Yin, G.Z.; Wan, L.; Shen, L.Y. Case history of controlling a landslide at Panluo open-pit mine in China. *Environ. Geol.* **2008**, *54*, 699–709. [[CrossRef](#)]
6. Nie, L.; Li, Z.C.; Lv, Y.; Wang, H.F. A new prediction model for rock slope failure time: A case study in West Open-Pit mine, Fushun, China. *Bull. Eng. Geol. Environ.* **2017**, *76*, 975–988. [[CrossRef](#)]
7. Zhang, F.; Yang, T.H.; Li, L.C.; Zhu, X.P. Investigation on the Reinforcement Effect of a Bedding Slope Affected by a Landsliding Block. *Arab. J. Geosci.* **2022**, *15*, 528. [[CrossRef](#)]
8. An, B.; Zhu, C.; Liu, K.M.; Li, S.T.; Tao, Z.G.; Li, H.P.; Yu, H.R. The Influence of Rainfall on Landslide Stability of an Open-Pit Mine: The Case of Haizhou Open-Pit Mine. *Geotech. Geol. Eng.* **2019**, *37*, 3367–3378. [[CrossRef](#)]
9. Kang, K.; Fomenkp, I.K.; Wang, J.; Nikolskaya, O.V. Probabilistic Assessment of Rock Slope Stability in Open Pit Mine Chaarat using the Generalized Hoke-Brown Criterion. *J. Min. Sci.* **2020**, *56*, 732–740. [[CrossRef](#)]
10. Troncone, E.; Conte, E.; Donato, A. Two and three-dimensional numerical analysis of the progressive failure that occurred in an excavation-induced landslide. *Eng. Geol.* **2014**, *183*, 265–275. [[CrossRef](#)]
11. Dhahri, F.; Benassi, R.; Mhamdi, A.; Zeyeni, K.; Boukadi, N. Structural and geomorphological controls of the present-day landslide in the Moulares phosphate mines (western-central Tunisia). *Bull. Eng. Geol. Environ.* **2016**, *75*, 1459–1468. [[CrossRef](#)]
12. Sun, S.-W.; Pang, B.; Hu, J.-B.; Yang, Z.X.; Zhong, X.Y. Characteristics and mechanism of a landslide at Anqian iron mine, China. *Landslides* **2021**, *18*, 2593–2607. [[CrossRef](#)]
13. Sun, G.M.; Hu, G.J.; Xiao, P.; Wang, X.F. Study on strength calculation and quality grading of slope rock in Fushun West Open Pit Mine. *Coal Sci. Technol.* **2017**, *45*, 36–41, 63. (In Chinese) [[CrossRef](#)]
14. Gao, B. North Slope Landslide Analysis and Control Research in Fushun West Open-pit Mine. *Opencast Min. Technol.* **2017**, *32*, 14–16, 20. (In Chinese) [[CrossRef](#)]
15. Segomo, S.; Piciullo, L.; Gariano, S.L. A review of the recent literature on rainfall thresholds for landslide occurrence. *Landslides* **2018**, *15*, 1483–1501. [[CrossRef](#)]
16. Liu, D.Y.; Wang, E.D.; Song, J.C.; Zhang, C.S. The Relation between Landslide and Rainfall and Prediction Method of Western Open-pit Coal Mine of Fushun. *J. Catal.* **2008**, *23*, 50–54. (In Chinese) [[CrossRef](#)]
17. Bossi, G.; Zabuski, L.; Pasuto, A.; Marcato, G. Capabilities of Continuous and Discontinuous Modelling of a Complex, Structurally Controlled Landslide. *Geotech. Geol. Eng.* **2016**, *34*, 1677–1686. [[CrossRef](#)]
18. Ji, Y.S.; (China Coal Technology & Engineering Group Shenyang Research Institute, Shenyang, China); Shen, L.; (China Coal Technology & Engineering Group Shenyang Research Institute, Shenyang, China); Liu, J.H.; (China Coal Technology & Engineering Group Shenyang Research Institute, Shenyang, China). Personal communication: Surface Stability Evaluation of Fushun No.1 Petroleum Plant, Power Plant and Cement Plant, 2015. (In Chinese)
19. Sun, S.W.; Liu, L.; Hu, J.B.; Ding, H. Failure characteristics and mechanism of a rain-triggered landslide in the northern longwall of Fushun west open pit, China. *Landslides* **2022**, *19*, 2439–2458. [[CrossRef](#)]
20. Cui, Q.; Zhang, L.; Chen, X.; Cao, Z.J.; Zhang, J.; Xu, J.B.; Liu, D.S.; Du, C.L. Quantitative risk assessment of landslides with direct simulation of pre-failure to post-failure behaviors. *Acta Geotech.* **2022**, *17*, 4497–4514. [[CrossRef](#)]
21. Iverson, R.M.; Ouyang, C.J. Entrainment of bed material by Earth-surface mass flows: Review and reformulation of depth-integrated theory. *Rev. Geophys.* **2015**, *53*, 27–58. [[CrossRef](#)]
22. Ouyang, C.J.; He, S.M.; Xu, Q.; Luo, Y.; Zhang, W.C. A MacCormack-TVD finite difference method to simulate the mass flow in mountainous terrain with variable computational domain. *Comput. Geosci.* **2013**, *52*, 1–10. [[CrossRef](#)]
23. Ouyang, C.J.; An, H.C.; Zhou, S.; Wang, Z.W.; Su, P.C.; Wang, D.P.; Cheng, D.X.; She, J.X. Insights from the failure and dynamic characteristics of two sequential landslides at Baige village along the Jinsha River, China. *Landslides* **2019**, *16*, 1397–1414. [[CrossRef](#)]
24. Zhou, Q.; Xu, Q.; Peng, D.L.; Fan, X.M.; Ouyang, C.J.; Zhao, K.Y.; Li, H.J.; Zhu, X. Quantitative spatial distribution model of site-specific loess landslides on the Heifangtai terrace, China. *Landslides* **2021**, *18*, 1163–1176. [[CrossRef](#)]
25. Scaringi, G.; Fan, X.M.; Xu, Q.; Liu, C.; Ouyang, C.J.; Domènech, G.; Yang, F.; Dai, L.X. Some considerations on the use of numerical methods to simulate past landslides and possible new failures: The case of the recent Xinmo landslide (Sichuan, China). *Landslides* **2018**, *15*, 1359–1375. [[CrossRef](#)]
26. Gao, Y.; Yin, Y.P.; Li, B.; Feng, Z.; Wang, W.P.; Zhang, N.; Xing, A.G. Characteristics and numerical runout modeling of the heavy rainfall-induced catastrophic landslide–debris flow at Sanxicun, Dujiangyan, China, following the Wenchuan Ms 8.0 earthquake. *Landslides* **2017**, *14*, 1361–1374. [[CrossRef](#)]

**Disclaimer/Publisher’s Note:** The statements, opinions and data contained in all publications are solely those of the individual author(s) and contributor(s) and not of MDPI and/or the editor(s). MDPI and/or the editor(s) disclaim responsibility for any injury to people or property resulting from any ideas, methods, instructions or products referred to in the content.